Single-photon-level narrowband memory in a hollow-core photonic bandgap fiber

Thorsten Peters, Ta-Pang Wang, Antje Neumann, Lachezar S Simeonov, Thomas Halfmann

Research Article | Vol. 28, No. 4 / 17 February 2020 / Optics Express 5340
Optics EXPRESS

Single-photon-level narrowband memory in a hollow-core photonic bandgap fiber

THORSTEN PETERS,[1,*] TA-PANG WANG,[1] ANTJE NEUMANN,[1] LACHEZAR S. SIMEONOV,[2] AND THOMAS HALFMANN[1]

[1]Institut für Angewandte Physik, Technische Universität Darmstadt, Hochschulstrasse 6, 64289 Darmstadt, Germany
[2]Department of Physics, Saint Kliment Ohridski University of Sofia, 5 James Bourchier Boulevard, 1164 Sofia, Bulgaria
[*]thorsten.peters@physik.tu-darmstadt.de

Abstract: An experimental platform operating at the level of individual quanta and providing strong light-matter coupling is a key requirement for quantum information processing. In our work, we show that hollow-core photonic bandgap fibers filled with laser-cooled atoms might serve as such a platform, despite their typical complicated birefringence properties. To this end, we present a detailed theoretical and experimental study to identify a fiber with suitable properties to achieve operation at the single-photon level. In the fiber, we demonstrate the storage and on-demand retrieval as well as the creation of stationary light pulses, based on electromagnetically induced transparency, for weak coherent light pulses down to the single-photon level with an unconditional noise floor of 0.017(4) photons per pulse. These results clearly demonstrate the prospects of such a fiber-based platform for applications in quantum information networks.

1. Introduction

Optical quantum information processing [1] requires generation, processing and detection of individual photons. Huge efforts have been dedicated to building high-brightness single-photon sources [2], implementing efficient quantum memories [3,4], and developing schemes to provide strong light-matter coupling, allowing for interactions between individual photons [5].

A powerful approach towards high memory efficiency [6] and interaction between photons is based on electromagnetically induced transparency (EIT) in atomic ensembles [7]. EIT permits reversible group velocity control, e.g., for light storage and retrieval (LSR) [7] with on-demand readout, stationary light pulses (SLPs) [8], as well as interactions between light fields via a Kerr-type nonlinearity [9–11]. SLPs are of particular interest due to their potential for nonlinear optics at the few-photon level [11–13] and studying many-body physics with light [14]. Although an EIT-driven memory and SLPs with non-classical quantum states were demonstrated in free-space cold atomic ensembles [15–17], demonstrations of nonlinear optical interactions were so far restricted to classical light pulses of large average photon number $\bar{n}$ [18]. Large nonlinearities require that two photons interact with the same atom simultaneously, which can be quantified by the optical depth per atom $d^*_{opt} = \sigma_0/\pi w_0^2$ [5], where σ_0 is the atomic absorption cross-section and w_0 is the waist of the Gaussian beam. This requires very tight focusing of the laser beams and thus results in small interaction volumes in free-space setups and, hence, small optical depths $d_{opt} = \sigma_0 nL$, where n is the atomic number density and L is roughly given by the Rayleigh length. As the coupling strength of light to atomic ensembles as well as the LSR efficiency is proportional to the optical depth d_{opt} [19], experimental setups are required that provide both large d_{opt} and d^*_{opt}. Therefore, in recent years there have been efforts to couple atomic ensembles to waveguides such as hollow-core fibers [20–24], tapered optical nanofibers [25], and nanoscale photonic crystals [26], which allow for tight transversal confinement of light and atoms over macroscopic distances.

#383999 https://doi.org/10.1364/OE.383999
Journal © 2020 Received 26 Nov 2019; revised 16 Jan 2020; accepted 18 Jan 2020; published 12 Feb 2020

Optics EXPRESS

So far, single-photon-level SLPs have not been demonstrated in fiber-coupled atomic ensembles while single-photon-level LSR was demonstrated for broadband photons employing a Raman protocol with room-temperature atoms coupled to a large-core kagome-structured hollow-core fiber (core diameter 26 μm) [27], and for narrowband photons employing EIT with cold atoms coupled to optical nanofibers of sub-wavelength diameters [28,29]. While nanofibers provide a larger d^*_{opt} at the expense of smaller d_{opt} [28,29], reverse conditions occur in large-core kagome-structured hollow-core fibers [30,31]. Hence, a compromise is required, which provides larger d^*_{opt} than kagome-structured hollow-core fibers, while maintaining a large d_{opt}. Single-mode hollow-core photonic bandgap fibers (HCPBGFs) [32] with core diameters below 10 μm, $d_{opt} \lesssim 1000$ and $d^*_{opt} \sim 4 \times 10^{-3}$ [33] can reach this goal. However, in contrast to nano- and kagome-type fibers, which can propagate a (quasi-)linearly polarized mode [34,35], HCPBGFs show uncontrolled coupling between transverse and polarization modes [36]. This is an obstacle for applications, when polarization control is required. The latter is the case in storage protocols involving polarization filtering of a strong collinear control beam, e.g., as required for on-demand readout of a quantum memory. Hence, we require fiber designs, which preserve the polarization upon low-loss propagation [36,37]. To the best of our knowledge, controlled fabrication of a polarization maintaining (PM) HCPBGF, has only been realized for a large-core fiber [36]. For smaller core diameters, only unintentional deformations during the drawing process were shown to lead to large linear birefringence as in PM fibers [38].

In our work we demonstrate that, despite the difficulties arising from uncontrolled birefringence in HCPBGFs, these fibers may serve as an efficient platform for optical quantum information processing. To this end, we store and retrieve narrowband coherent light pulses on-demand, and create SLPs down to the single-photon level in an ensemble of laser-cooled atoms loaded into a HCPBGF of core diameter (5.5 − 7.0) μm with a $d^*_{opt} \sim 1.7 \times 10^{-3}$. Compared to our previous work, limited to operation at still rather large mean photon numbers beyond $\bar{n} \sim 70$ due to polarization issues [39], we mainly achieved this milestone by identifying a suitable HCPBGF via a thorough theoretical and experimental analysis of its complicated birefringence properties. Furthermore, by applying a different fine structure transition for the experiments, we achieved operation at lower control power, as well as reduced off-resonant absorption and inhomogeneous ac Stark shifts. With an increased efficiency and improved signal-to-noise ratio (SNR) by roughly two orders of magnitude, we perform a first systematic study of optimum conditions for SLPs in a waveguide.

2. Birefringence characterization of a HCPBGF

HCPBGFs can be produced with core diameters below 10 μm, approaching values of d^*_{opt} close to the case of nanofibers. However, they normally show large uncontrolled birefringence [36,38,40], which is typically due to structural defects close to the core, with dimensions much smaller than the periodicity of the HCPBGF cladding structure [41]. So far, there has only been a demonstration of a PM HCPBGF for a large core diameter [36]. To the best of our knowledge, HCPBGFs of core diameter <10 μm, with large transmission and good PM properties, are currently not available. Therefore, we have to stick with the available HCPBGFs, carefully analyze their birefringence properties, and optimize the experimental conditions for applications using these fibers. Thus, in the following we present a detailed analysis to identify a suitable commercial fiber for experiments at the quantum level.

A detailed theoretical analysis of the polarization properties of light transmitted through a HCPBGF, including linear ϕ and circular birefringence χ, is presented in the Appendix A. There we show that by measuring the orientation θ' of the output field's main axis, given by

$$\theta' = \mathrm{Re}\left[\arctan\left(\frac{\mathcal{E}_y(\tilde{\theta},\phi,\chi)}{\mathcal{E}_x(\tilde{\theta},\phi,\chi)}\right)\right] + \beta, \tag{1}$$

Optics EXPRESS

and the degree of linear polarization (DOP), given by

$$\mathrm{DOP} = \sqrt{1 - 4\cos^2\chi \sin^2\frac{\phi}{2}\left(\sin 2\tilde{\theta}\cos\frac{\phi}{2} + \cos 2\tilde{\theta}\sin\frac{\phi}{2}\sin\chi\right)^2}, \tag{2}$$

we obtain the linear and circular birefringence properties ϕ and χ, respectively, as well as the orientation β of the optical axis in the fiber [see Fig. 1(b)]. Here, $\tilde{\theta} = \theta - \beta$ and $\mathcal{E}_{x,y}$ are the electric field amplitudes in the $(x, y)-$ directions. The angles θ, θ' and β are all measured with respect to the horizontal axis as shown in Fig. 1(b).

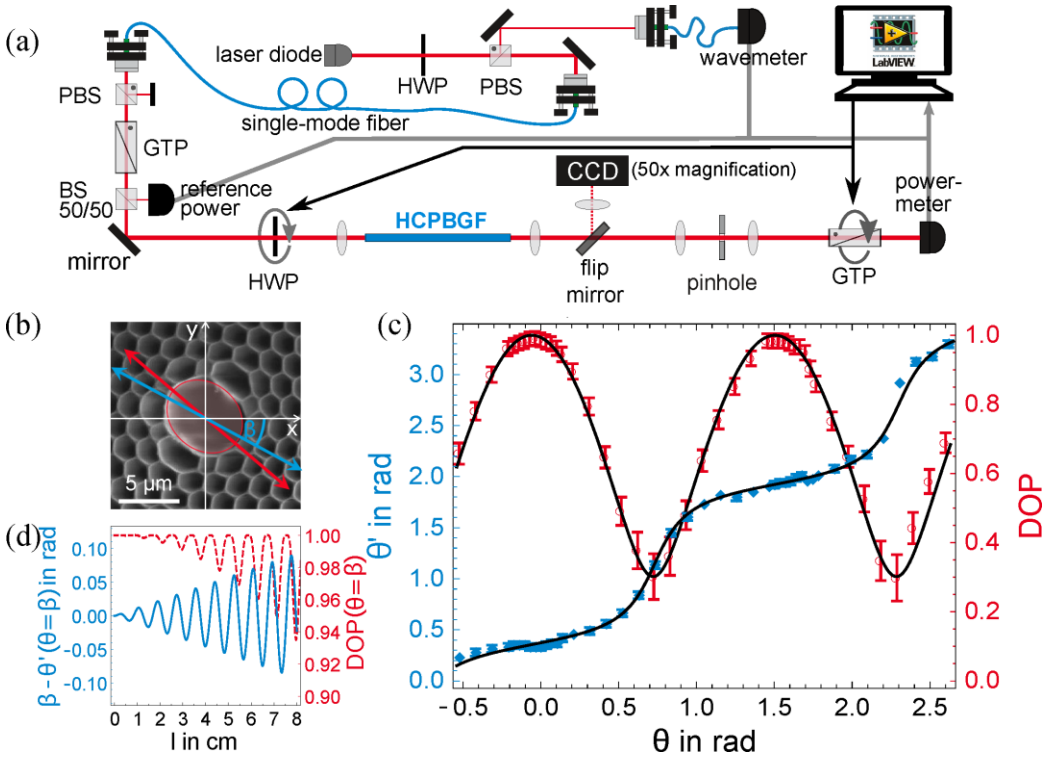

Fig. 1. (a) Schematic experimental setup for measuring the birefringence properties of a HCPBGF. PBS: polarizing beam splitter; GTP: Glan-Thompson polarizer; HWP: half-wave plate; BS: beam splitter. (b) Scanning electron image of the central region of our HCPBGF. The fiber core has an aspect ratio of about 0.8:1. The orientation of the optical axis β (blue) can differ from the main axis of the elliptical core (red). (c) Measured DOP (red) and output polarization direction θ' (blue) after the HCPBGF (symbols) as a function of linear input polarization direction θ for a wavelength of 780 nm. The black lines are simulations based on Eq. (1) and Eq. (2). (d) Calculated DOP (red) as a function of fiber length l and absolute rotation of the input polarization (blue) using the same parameters as in (c). For a length of $l \leq 3.5$ cm and an input angle $\theta = \beta$ the polarization can be maintained sufficiently well, if we assume DOP ≥ 0.99 and $\Delta\theta \leq 0.035$.

We thus study the DOP and the polarization direction θ' at the output of the HCPBGF as a function of linear input polarization direction θ. To this end, a piece of fiber is placed behind a polarizer and an adjustable half-wave plate, while the output polarization is determined with an adjustable polarizer (analyzer) [see Fig. 1(a)]. Starting with an almost perfectly linear-polarized input field [DOP = 0.999985(5)], the input orientation θ is aligned by an achromatic half-wave

Optics EXPRESS

plate (aHWP), which impairs the input polarization to DOP $\geq$ 0.9984. The angular dependence of the transmitted power $P(\vartheta)$ is analyzed with a Glan-Thompson polarizer and normalized to the input power P_0, resulting in $P(\vartheta)/P_0 = b + a\sin(\vartheta)$, where ϑ is the orientation of the analyzer. This yields DOP = a/b. The orientation θ' corresponds to the angular position of the maxima (or the position of minima offset by $\pi/2$, as the determination of the latter is more precise). Due to the excitation of surface modes it is important to make sure that only the approximately Gaussian-shaped mode transmitted through the core is analyzed. This can be achieved by spatial filtering using a pinhole. Higher-order modes that can propagate through the cladding zone considerably reduce the DOP.

The results for a commercial fiber (NKT Photonics HC-800-02) of length $l \approx 22\,\text{cm}$ and cross-section as shown in Fig. 1(b) are depicted in Fig. 1(c) for a wavelength of 780 nm. We find good agreement between the measured data (symbols) and the theory based on Eq. (1) and Eq. (2) (solid lines) for the values

$$\phi = 164.84(5), \quad \chi = 0.50(5), \quad \beta = 0.15(2).$$

All angles throughout this paper are given in radian. Note that in general both linear and circular birefringences ϕ and χ, respectively, are only defined by integer multiples of 2π. However, with a wavelength-sweeping technique [42], the exact value of ϕ can be determined. Hence, we require two measurements of the DOP for different wavelengths $\lambda_1 \neq \lambda_2$ with $\text{DOP}(\theta, \lambda_1) \approx \text{DOP}(\theta, \lambda_2)$. More details can be found in [42]. As the latter condition is not fulfilled for a fiber of length $l \approx 22\,\text{cm}$, we used a shorter fiber of length $l \approx 2\,\text{cm}$ to determine $\phi(l \approx 2\,\text{cm})$. We then extrapolated $\phi(l \approx 22\,\text{cm}) \approx \frac{22\,\text{cm}}{2\,\text{cm}}\phi(l \approx 2\,\text{cm}) = 167(1)$. This value is then used as a starting point to fit the theoretical dependence to the experimental data while slightly changing ϕ by $\pm 2\pi$. Here, the importance of the fit of $\theta'(\theta)$ becomes apparent. Only both fits together identify one unique ϕ in the given range. Regarding the circular birefringence χ, we characterized several fiber pieces of different lengths l and always obtained values for $\chi < \pi$ that scale linearly with l, thereby removing the uncertainty of $n2\pi$. Comparing the polarization beat length $L_b = 2\pi l/\phi = 8.0(8)\,\text{mm}$, to common glass fibers with typical L_b of several meters and PM fibers with L_b in the range of millimeters, in fact, we find our HCPBGF can be assigned rather to the latter kind. However, there are some twists.

The DOP obviously depends strongly on the input polarization orientation. The maximum $\text{DOP}_{\text{max}} = 0.9925(10)$ for an input orientation $\theta = -0.035(17)$ and output orientation $\theta' = 0.332(17)$ shows, that for certain input orientations, the HCPBGF can almost maintain the input DOP although the polarization is rotated in the lab frame. For purely linear birefringence ($\chi = 0$) the polarization direction would be maintained in the lab frame when the input polarization is aligned to the optical axis of the HCPBGF and the optimum DOP would be reached. However, when θ matches the optical axis $\beta = 0.15(2)$ we get DOP = 0.93(2) and $\theta' = 0.419(35)$, i.e., the polarization direction is rotated and the DOP is reduced. This is due to the circular birefringence $\chi \neq 0$. In Fig. 1(d) the deviation between output and input polarization direction for $\theta = \beta$ and the DOP is depicted as a function of the fiber length. For $l \lesssim 3.5\,\text{cm}$ we indeed can reach DOP $\geq$ 0.99 and the change of the orientation in the lab frame $\Delta\theta \leq 0.035$ is very small. For a fiber lengths $l \gtrsim 3.5$ cm a good DOP can be maintained only by choosing a different input polarization orientation $\theta \neq \beta$, which is necessary due to the small circular birefringence of our fiber. We specifically note that this optimum input orientation neither coincides with the HCPBGF's geometric main axis [red arrow in Fig. 1(b)], nor with the measured optical axis orientation β. This clearly illustrates the importance of a careful characterization of the polarization properties of such HCPBGFs before applying them in experiments.

Finally, inspection of both fiber facets by a microscope lead to the surprising finding that the fiber has an intrinsic twist of 0.068(52)/cm. The optical axis is therefore rotating along the fiber length. We compensated this by untwisting the fiber for the measurements shown in Fig. 1.

Optics EXPRESS

Other measurements (not shown here) for different external twists up to π showed that the twists are still too small to affect the measured birefringences ϕ and χ. Such twists of angle α, however, have to be considered in Eq. (1) by adding $\theta^{'} + \alpha$.

Also measurements at a wavelength of 787 nm yielded similar birefringence values [ϕ = 166.08(7), χ = 0.18(5)], i.e., the predominantly linear birefringence is maintained over a wavelength range of at least several nanometers. This dominating linear birefringence of our fiber is probably due to the elliptical core with an aspect ratio of around 0.8:1 [41] and/or the two larger holes in the first ring of the cladding. Without this large asymmetry, the birefringence properties might be even more complex [40] and we would not be able to maintain the linear polarizations of the laser beams as they propagate through the HCPBGF. This would inhibit efficient polarization filtering at the output and prevent using the HCPBGF for experiments at the single-photon level that we will discuss in the remaining part of this paper.

3. Experimental setup

We now turn to a presentation of the experiments on LSR and SLPs using the previously characterized HCPBGF. The schematic experimental setup is shown in Fig. 2(a). We implement the experiment with cold ^{87}Rb atoms, loaded from a magneto-optical trap (MOT) into the HCPBGF, involving a far off-resonant optical trap (FORT) to guide the atoms inside the fiber and prevent collisions with the room-temperature fiber wall [33]. The FORT laser system uses two superimposed orthogonally-polarized laser diode beams at 820 nm. With a trapping power of 110 mW inside the HCPBGF, we obtain a trap depth of around 4 mK. The probe laser is locked with an offset of 76 MHz to the transition $5^2S_{1/2}$, $F = 1 \leftrightarrow 5^2P_{1/2}$, $F^{'} = 1$ via bichromatic saturation absorption spectroscopy [43]. The control laser is phase-locked to the probe yielding a two-photon linewidth of $\sim$ 8 kHz [see coupling scheme in Fig. 2(b)]. Acousto-optic modulators (AOMs) modulate the laser beam intensities and shift the frequencies to the required detuning. Probe and control fields have orthogonal linear polarizations, which are launched into the HCPBGF such that the strong control is best suppressed at the detector. To adjust the linear polarizations of all fields inside the HCPBGF at wavelengths of 780 nm, 795 nm, and 820 nm, we use aHWPs. We suppress the direct background noise of the control beam collinear to the probe by frequency filtering using a monolithic etalon [44] with an attenuation of $\sim$ 45 dB and by polarization filtering, aligning the input polarizations to the HCPBGF according to the results in Sec. 2. This attenuates the control beam by up to 86 dB. Working on the D_1 instead of the D_2 line with a larger transition strength for the control field, we gain another 8 dB in background noise suppression while maintaining a large Rabi frequency, with much reduced ac Stark shifts by off-resonant levels. This yields a total background noise reduction of 20 dB compared to our previous work.

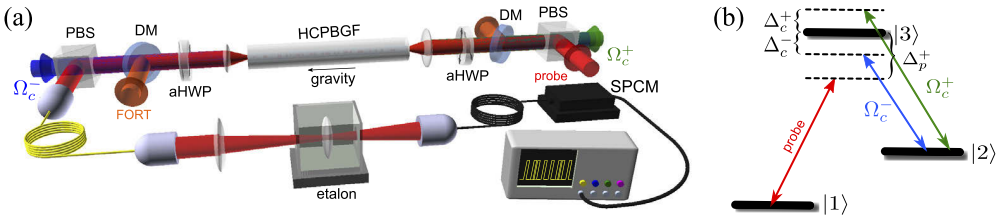

Fig. 2. (a) Simplified experimental setup. PBS: polarizing beam splitter, DM: dichroic mirror, SPCM: single-photon counting module. (b) Level scheme for EIT-based LSR and SLPs. $|1, 2\rangle = 5^2S_{1/2}$, $F = 1, 2$, and $|3\rangle = 5^2P_{1/2}$, $F^{'} = 1$.

Optics EXPRESS

The transmission of the probe beam from the HCPBGF to the detector is 0.13(1). We detect the transmitted photons by a single-photon counting module (SPCM, PerkinElmer, SPCM-AQRH-12). The TTL output pulses of the SPCM are recorded with a digital oscilloscope of 100 MHz bandwidth. The oscilloscope is triggered by the start of the first probe pulse. All events are then recorded during one measurement sequence lasting 200 μs (corresponding to 50 measurement windows separated by 4 μs) where the FORT is modulated for each single HCPBGF loading cycle (see Appendix B.). The temporally resolved transmission signal is then generated via software analysis by slicing the data into bins of 30 ns width and averaging over the different measurement time slots as well as 60 different HCPBGF loading cycles, leading to a total of 1500 averages. The same applies to the background signal which is subtracted from the recorded data.

For more experimental details such as the sequences for loading the HCPBGF and the measurements see [33,39] and the Appendix B.

4. Experimental results

4.1. Light storage and retrieval of coherent light pulses

In order to demonstrate that the here used HCPBGF is suitable for a quantum memory with on-demand readout, we now turn to EIT-based LSR. The coupling scheme is shown in Fig. 2(b), where only the forward control field Ω_c^+, collinear to the probe, is switched on, while the backward control field $\Omega_c^- \equiv 0$. Details on the LSR pulse sequence can be found in the Appendix B. EIT creates dark-state polaritons (DSPs) with a moving photonic and a non-moving atomic coherence between states $|1\rangle$ and $|2\rangle$ [45]. The group velocity of the DSPs can be controlled by Ω_c^+. Ramping Ω_c^+ adiabatically down to zero maps the photonic DSP component onto the non-moving atomic component. By ramping the control field back up, the coherence is retrieved on-demand into a moving light pulse [46]. We modulate the control field with an AOM to produce storage periods of variable duration τ_{LSR}. The measured transmissions for $\tau_{LSR} = 200$ ns and $\tau_{LSR} = 500$ ns are shown in Fig. 3 in dark blue and red, respectively, for Gaussian probe pulses of $1/e$ full width $\tau_p = 150(2)$ ns and $\bar{n} = 17(3)$ photons per input pulse. Here, $\bar{n}$ is the average photon number per input pulse as seen by the atoms and accounting for the non-perfect detection efficiency of 0.13(1).

For reference we show the input probe pulse without atoms loaded into the HCPBGF and a slow light pulse with constant control Rabi frequency in black and gray, respectively. The solid lines represent Gaussian least-squares fits to the experimental data. From these fits we obtain a LSR efficiency of $\eta_{LSR} = [0.51(4); 0.36(4); 0.25(3)]$ for storage times of $\tau_{LSR} = [0; 200; 500]$ ns, respectively. By analyzing the retrieval efficiency vs. storage time and fitting the data with an exponential decay we obtain a decay rate of $\gamma_{21} = 0.26(2)\Gamma$. This is larger than the value reported in [39] and could be due to an inhomogeneous magnetic field present inside the fiber or be related to the larger than expected absorption (see Sec. 4.3). In the same figure we also plot the results for LSR with coherent input pulses containing $\bar{n} = 1.1(2)$ photons (light blue and red). There is very good agreement between the pulses at the single-photon level and those with higher photon numbers. This clearly demonstrates that HCPCBGs filled with cold atoms can serve as an optical memory at the quantum level. The unconditional noise floor is $\bar{n}_{noise} \ll 1$ photon per pulse (see detailed discussion in Sec. 4.3).

4.2. Stationary light pulses

LSR allows for the stopping of light pulses. However, as the photons are converted into atomic coherences, no light is inside the medium during the storage period, prohibiting nonlinear optical interactions. In order to reduce the group velocity of the DSPs to zero while maintaining a photonic component (i.e., a light pulse), a second counter-propagating control beam of Rabi frequency Ω_c^- can be added while the probe pulse is propagating through the medium driven by

Optics EXPRESS

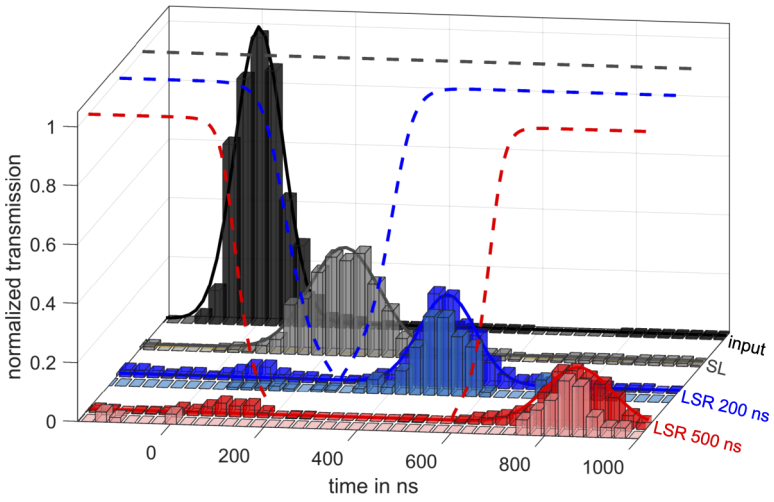

Fig. 3. Demonstration of LSR down to the single-photon level. Measured normalized transmission (bars) through the HCPBGF vs. time for input pulses (black) containing $\bar{n} = 17(3)$ photons, slow light (SL) (gray), and LSR for $\tau_{LSR} = 200$ ns (blue) and $\tau_{LSR} = 500$ ns (red). The light blue and red bars correspond to $\bar{n} = 1.1(2)$ photons per input probe pulse as seen by the atoms. The solid colored lines are Gaussian least-squares fits to the corresponding experimental data. The dashed colored lines schematically show the corresponding timing of $\Omega_c^+(t)$. All experimental data are scaled with respect to the fit amplitude of the input pulse. The parameters are: $\Omega_c = 3.6(2)\Gamma$, $d_{opt} = 109(10)$, $\Delta\omega_{EIT} = 1.2\Gamma$.

the co-propagating control beam of Rabi frequency Ω_c^+ [47]. This creates an all-optical cavity for the probe pulse and a SLP with a quasi-stationary envelope is formed. Due to the non-vanishing photonic component of the formed DSPs, nonlinear optical interactions are now possible [11–13]. We therefore demonstrate in the following that also SLPs can be created in a HCPBGF at the single-photon level. Details on the SLP sequence can be found in the Appendix B. In order to keep the effective group velocity $v_{gr} \propto \Omega_0^2$ with $\Omega_0^2 = (\Omega_c^+)^2 + (\Omega_c^-)^2$ [48] of the DSPs almost constant during the whole experiment, we reduce Ω_c^+ during the SLP period τ_{SLP}, when Ω_c^- is on. This allows for a better comparison with SL data, where $\Omega_c^- \equiv 0$. Without keeping Ω_0^2 constant, the effective DSP group velocity would be more than doubled during τ_{SLP}.

In Fig. 4(a) we compare the transmission through the HCPBGF for four different conditions. Without atoms loaded into the fiber the input pulse (black, scaled down by a factor of 0.2 for better comparison) is transmitted as a reference. When $\Omega_c^- \equiv 0$ and Ω_c^+ is modulated according to the gray dashed line, we observe a spread-out probe pulse due to the much reduced group velocity during $\Delta t_{SLP} = 150$ ns $\lesssim t \lesssim 650$ ns (gray bars). When the backward control field (magenta dotted line) is much stronger than the forward control (magenta dashed line) during Δt_{SLP}, with $\Omega_c^-/\Omega_c^+ = 1.84$, we observe basically no transmission during Δt_{SLP} and only a very small retrieved probe signal after the backward control is switched off (magenta bars). This small signal in addition is delayed with respect to the switch-off time of the backward control field. The delayed read-out can be well-explained by considering the SLP group velocity $v_{gr}^{SLP} = v_{gr} \cos 2\phi$ with $\tan^2\phi = |\Omega_c^-|^2/|\Omega_c^+|^2$ [48]. For $\Omega_c^-/\Omega_c^+ = 1.84$ the SLP propagates backward at around $-0.55 \times v_{gr}$ during Δt_{SLP} and thus exits the medium at later times during the retrieval in the forward direction. In contrast, when Ω_c^+ and Ω_c^- are nearly balanced for optimum SLP conditions (blue dashed and dotted lines), there is some leakage of light during τ_{SLP} [but reduced compared to SL (gray bars)] and a significantly larger retrieved probe pulse area after the backward control

Optics EXPRESS

is switched off (blue bars). This is the typical signature of a SLP having a non-vanishing intensity at the edges of the medium and therefore showing leakage [17,39,47,49]. The probe signal for times $t \lesssim 150$ ns apparent in the gray, blue and magenta data sets corresponds to the rising edge of the probe pulses which have already left the medium before the SLP period starts.

As noticed in our previous work on SLPs in a HCPBGF [39], we obtain the largest SLP retrieval efficiency for $\Omega_c^- > \Omega_c^+$. This is in contrast to free-space setups, where balanced control fields are typically used [17,49,50]. Due to the small retrieval efficiency and limited SNR, we previously were unable perform a systematic study of η_{SLP} as a function of the ratio Ω_c^-/Ω_c^+ during τ_{SLP}, where η_{SLP} is the relative pulse area retrieved after the SLP period is over. With the much improved retrieval efficiency and SNR in the present work, we can now study this dependence. Figure 4(b) shows the results. We clearly obtain the largest SLP retrieval efficiency after Δt_{SLP}, when $\Omega_c^- \sim 1.2 \times \Omega_c^+$ during Δt_{SLP}, i.e., not for balanced control Rabi frequencies (dashed vertical line). We believe that this is due to the phase-mismatch [see Fig. 4(c) and [39]]. The backward probe field experiences larger attenuation than the forward probe due to the phase-mismatch $2\omega_{21}/c$, where ω_{21} is the hyperfine splitting of the ground states $|1\rangle$ and $|2\rangle$. By choosing a larger Ω_c^-, this phase-mismatch can be compensated to some extend by a stronger excitation of the backward propagating mode. The maximum SLP retrieval efficiency we obtain is $\eta_{SLP} = 0.16(2)$, i.e., a five-fold improvement compared to our previous work [39]. Therefore, η_{SLP} is now of the same order as the corresponding η_{LSR} (see Sec.4.1).

Finally, we consider the generation of SLPs at the single-photon level. SLPs are promising candidates to achieve nonlinear optical interactions at the quantum level. To this end, we compare in Fig. 5 the results for weak coherent input pulses containing $\bar{n} = 10(2)$ (dark blue) to $\bar{n} = 1.9(4)$ photons (light blue) and $\bar{n} = 5(1)$ (dark red) to $\bar{n} = 1.1(2)$ photons (light red) from a different experimental run. The efficiencies η_{SLP} for higher and lower $\bar{n}$ agree with each other within 3% for each experimental run, demonstrating that also single-photon level SLPs can be generated and detected in a HCPBGF. The background noise, obtained by blocking the input probe pulse while keeping everything else the same, is shown for reference in green. This background corresponds to an unconditional noise floor of $\bar{n}_{noise} = 0.017(4)$ photons per pulse.

4.3. Discussion

The measured unconditional noise floor $\bar{n}_{noise}$ for the SLP sequence is much lower than one photon per pulse and slightly larger than for the LSR sequence, where the medium is driven by a single control beam only. Therefore, our HCPBGF filled with laser-cooled atoms is a promising platform for EIT-based quantum information processing without post-selection. Compared to the Raman memory in [27], $\bar{n}_{noise}$ obtained in our setup is significantly lower, as we apply cold atoms and resonant interactions. Compared to a nanofiber-based EIT-memory [28], our noise floor is comparable. It is worth briefly discussing the (possible) origins of noise in our setup. Currently, the main contributions are stray light entering the fiber to the SPCM (1×10^{-2} photons per pulse) and SPCM dark counts (4×10^{-3} photons per pulse) These are simply technical issues, which permit further improvement – if required. With the findings on the birefringence discussed in Sec. 2. leading to a control suppression of 86 dB by polarization and frequency filtering, a direct contribution of control photons to $\bar{n}_{noise}$ can be estimated as 4×10^{-4} photons per pulse and is therefore negligible. Also, noise induced by spontaneous four-wave mixing [51], as observed in [27], due to the control off-resonantly driving the transition $|1\rangle \leftrightarrow |3\rangle$ seems to play a minor role. Otherwise, the background noise shown in Fig. 5 would depend upon the control Rabi frequency – which we did not observe. Besides these possible contributions we could identify the proper preparation of the population in the ground state as a strong contributor to the noise floor. In addition to the control beam driving the transition $5^2S_{1/2}$, $F = 2 \leftrightarrow 5^2P_{1/2}$, $F' = 1$ and preparing the population in $|1\rangle$, we applied a pump beam, off-resonantly driving the transition $5^2S_{1/2}$, $F = 2 \leftrightarrow 5^2P_{3/2}$, $F' = 2$ to reduce the noise to the level shown in Fig. 5.

Optics EXPRESS

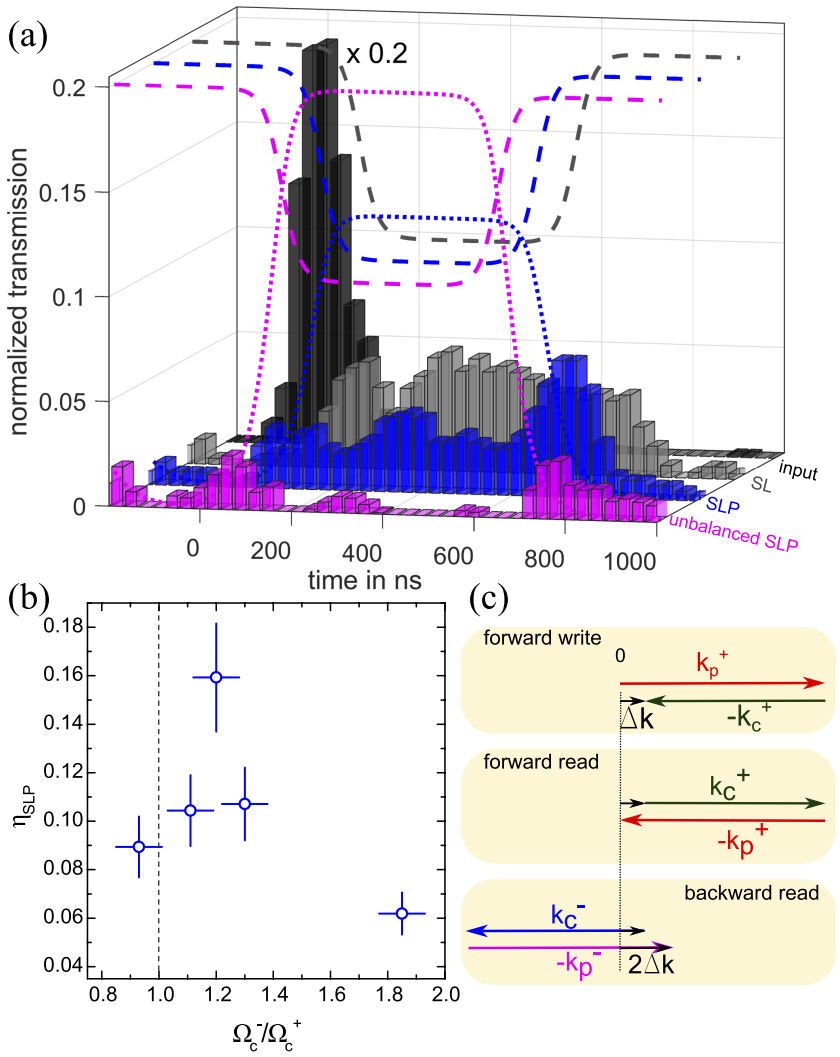

Fig. 4. (a) Study of SLPs inside a fiber. We show the measured normalized transmission (bars) through the HCPBGF vs. time. The Gaussian input pulse [black; scaled down by a factor of 0.2 in (a)] is measured without atoms inside the HCPBGF. All experimental data is scaled with respect to the fit amplitude of the input pulse. SL (gray) with a modulated Ω_c^+ (gray dashed); SLP (blue) for Ω_c^+ (blue dashed) and Ω_c^- (blue dotted) slightly unbalanced during τ_{SLP}; backward propagating quasi-SLP (magenta) for Ω_c^+ (magenta dashed) and Ω_c^- (magenta dotted) strongly unbalanced during τ_{SLP}. (b) SLP retrieval efficiency η_{SLP} vs. the ratio Ω_c^-/Ω_c^+ during the SLP period. The vertical dashed line marks the case of perfectly balanced forward and backward control Rabi frequencies. (c) Wavevector diagram showing the phase-mismatch $\Delta k = 2\pi \cdot 6.835$ GHz/c for forward light storage, $\Delta k = 0$ for forward readout, and $\Delta k = 2 \times 2\pi \cdot 6.835$ GHz/c for backward readout. $k_{p,c}^{\pm}$ are the wavevectors of the probe and control fields in the forward (+) and backward (−) directions. The parameters are: $d_{opt} \sim 80(5)$, $\Omega_c^+ = 3.5(2)\Gamma$ (gray, blue, magenta dashed), $\Omega_c^- = [2.3(2); 3.5(2)]\Gamma$ [(blue; magenta) dotted], $\Delta_p^+ = \Delta_c^+ = 0$, $\Delta_c^- = +2.5\Gamma$, $\tau_{SLP} = 500$ ns. Note that the Rabi frequencies given correspond to maximum values of the dashed and dotted curves, respectively.

Optics EXPRESS

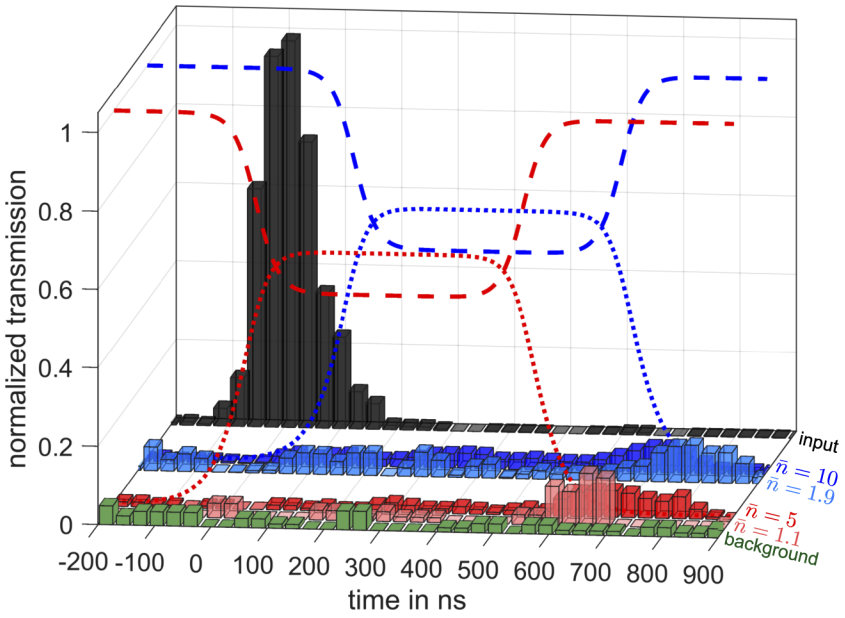

Fig. 5. Demonstration of SLPs down to the single-photon level. The Gaussian input pulse (black) without atoms inside the HCPBGF is shown for reference. SLPs are shown for $\bar{n} = 10(2)$ [blue; same data as in Fig. 4(a)] and $\bar{n} = 1.9(4)$ photons per pulse (light blue). Other experimental run for $\bar{n} = 5(1)$ (red) and $\bar{n} = 1.1(2)$ photons per pulse (light red) as seen by the atoms where the control timing was shifted by −115 ns compared to the blue data. The background noise, when the input probe pulse is blocked, is shown in green. The parameters are: $d_{opt} \sim 80(5)$ (blue), $d_{opt} \sim 70(5)$ (red), $\Omega_c^+ = 3.5(2)\Gamma$ (blue dashed), $\Omega_c^- = 2.3(2)\Gamma$ (blue dotted), $\Omega_c^+ = 3.0(2)\Gamma$ (red dashed), $\Omega_c^- = 2.4(2)\Gamma$ (red dotted) $\Delta_p^+ = \Delta_c^+ = 0$, $\Delta_c^- = +2.5\Gamma$, $\tau_{SLP} = 500$ ns. Note that the Rabi frequencies given correspond to maximum values of the dashed and dotted curves, respectively.

Our measured LSR efficiency is comparable to the Raman memory in [27] but significantly larger compared to related work [28,29] in nanofibers, due to the higher d_{opt} (but lower d^*_{opt}) in our experiment. A comparison of SLP efficiencies to realizations in other waveguides is currently not possible as our current and previous results [39] represent at the moment the only demonstrations of SLPs in a waveguide geometry. Although our demonstrated LSR and SLP retrieval efficiencies are sufficient to reliably detect pulses at the single-photon level, we might expect $\eta_{LSR} \gtrsim 0.85$ for our $d_{opt} \sim 100$ [19]. To investigate this limited efficiency, we studied EIT spectra and compared the measured data to a numerical simulation including the radially varying control intensity and atomic density [39]. Detrimental effects due to (inhomogeneous) ac Stark shifts are much reduced at the D_1 compared to the D_2 line. However, the measured peak transmission is lower than expected from the simulation. For small EIT window widths $\Delta\omega_{EIT} = \Omega_c^2/\Gamma\sqrt{d_{opt}}$, where typically LSR and SLP experiments are performed, this larger absorption simply reduces efficiencies. For larger window widths, however, this reduced transmission is turned into a single low-transmission resonance within $\Delta\omega_{EIT}$, which we did not observe on the D_2 line for the same transition [39]. This issue is currently not understood and still under investigation. If solved, this should lead to even higher LSR and SLP efficiencies.

Optics EXPRESS

5. Summary and outlook

In summary, we demonstrated EIT-based LSR and SLPs for weak coherent light pulses containing as low as $\bar{n} = 1.1(2)$ photons per pulse, implemented in a medium of cold atoms inside a HCPBGF. We observed a LSR and SLP efficiency of up to 0.36(4) and 0.16(2), respectively, with an unconditional noise floor of $\bar{n}_{noise} = 0.017(4)$ photons per pulse. This was enabled, amongst others, by a careful characterization of a strongly birefringent HCPBGF, resulting in an efficient suppression of noise. With $d_{opt} \sim 100$ and $d^*_{opt} \sim 0.0017$, our results demonstrate the potential of HCPBGFs loaded with laser-cooled atoms as an optical memory operating at the quantum level, while simultaneously providing strong light-matter coupling. Combining our results with the recent demonstrations of magic-wavelength trapping [52,53] and coherent guiding [54] in hollow-core fibers or the realization of fiber-integrated cavities [55] we expect HCPBGF-based platforms loaded with cold atoms to provide exciting possibilities for quantum information networks.

Appendix

A. Theoretical analysis of the birefringence of a HCPBGF

In analogy to common glass fibers, the HCPBGF used in our experiment, is supposed to be highly birefringent due to the geometric asymmetry of the elliptic core and the additional symmetry breaking structural elements inside the cladding zone next to the core [38,40]. To model the birefringence of the fiber, we assume an in general elliptical birefringence with linear and circular contributions. The initial light field is linearly polarized with real amplitude $\mathcal{E}_0$ and input orientation θ, oscillating in the x-y-plane

$$\vec{\mathcal{E}}(z=0) \equiv \vec{\mathcal{E}}_0 = \begin{pmatrix} \mathcal{E}_{0,x} \\ \mathcal{E}_{0,y} \end{pmatrix} = \begin{pmatrix} \mathcal{E}_0 \cos\theta \\ \mathcal{E}_0 \sin\theta \end{pmatrix}. \tag{3}$$

We use the Jones formalism with Jones matrix J to describe the effect of the birefringent fiber on the electromagnetic field

$$\vec{E}(z,t) = J\vec{E}(z=0,t), \qquad \vec{E}(z,t) = \mathrm{Re}\left[\vec{\mathcal{E}}(z)e^{-i\omega t}\right], \tag{4}$$

where we consider only the physically relevant real part. The Jones matrix J for elliptical birefringence reads [56,57]

$$J = \begin{pmatrix} \cos\frac{\phi}{2} - i\sin\frac{\phi}{2}\cos\chi & -\sin\frac{\phi}{2}\sin\chi \\ \sin\frac{\phi}{2}\sin\chi & \cos\frac{\phi}{2} + i\sin\frac{\phi}{2}\cos\chi \end{pmatrix}, \tag{5}$$

with ϕ defining the linear and χ the circular birefringence.

It is worth mentioning, that (5) provides a fixed main axis. However, in the case of a HCPBGF this theoretical main axis can differ from the geometrical main axis of the elliptical core [see Fig. 1(b)]. This can be possibly due to a change of its orientation over the fiber length, e.g., by an intrinsic torsion. We take this variation into account by adjusting the input angle $\tilde{\theta} = \theta - \beta$ with the orientation of the theoretical fixed main axis in relation to the horizontal axis β, visualized in Fig. 1(b).

Optics EXPRESS

To characterize the birefringence of the HCPBGF the orientation of the output field's main axis can be calculated with (see main document)

$$\theta' = \mathrm{Re}\left[\arctan\left(\frac{\mathcal{E}_y(\tilde{\theta},\phi,\chi)}{\mathcal{E}_x(\tilde{\theta},\phi,\chi)}\right)\right] + \beta \tag{6}$$

as well as the degree of linear polarization (DOP). In general this is given by the relation of the field intensity's maximum and minimum

$$\mathrm{DOP} = \frac{I_{\max} - I_{\min}}{I_{\max} + I_{\min}}, \tag{7}$$

with DOP = 1 for completely linear polarized light.

We would like to express DOP as a function of θ. Therefore, we first calculate the general form of $\vec{E}(z,t)$. By inserting (3) and (5) into (4) we get

$$E_x(z,t) = A\cos(-\omega t) + B\sin(-\omega t), \tag{8}$$

$$E_y(z,t) = C\cos(-\omega t) + D\sin(-\omega t), \tag{9}$$

with

$$A = \mathcal{E}_0\left[\cos\tilde{\theta}\cos\tfrac{\phi}{2} - \sin\tilde{\theta}\sin\chi\sin\tfrac{\phi}{2}\right], \tag{10}$$

$$B = -\mathcal{E}_0\cos\chi\sin\tfrac{\phi}{2}\cos\tilde{\theta}, \tag{11}$$

$$C = \mathcal{E}_0\left[\cos\tilde{\theta}\sin\tfrac{\phi}{2}\sin\chi + \sin\tilde{\theta}\cos\tfrac{\phi}{2}\right], \tag{12}$$

$$D = -\mathcal{E}_0\sin\tilde{\theta}\cos\chi\sin\tfrac{\phi}{2}. \tag{13}$$

$\vec{E}(z,t)$ fulfills the equation of a rotated ellipse

$$\frac{C^2+D^2}{\Delta^2}E_x^2 + \frac{A^2+B^2}{\Delta^2}E_y^2 - 2\frac{AC+BD}{\Delta^2}E_xE_y = 1, \tag{14}$$

with $\Delta = AD - BC$. To identify $I_{\max}$ and $I_{\min}$ we have to bring (14) to the normal form $r_1E_x^2 + r_2E_y^2 = 1$, because then

$$\mathrm{DOP} = \frac{r_2 - r_1}{r_2 + r1} = \sqrt{1 - \frac{4(AD-BC)^2}{A^2+B^2+C^2+D^2}}. \tag{15}$$

With $A^2 + B^2 + C^2 + D^2 = \mathcal{E}_0^2$ we finally obtain (see main document)

$$\mathrm{DOP} = \sqrt{1 - 4\cos^2\chi\sin^2\tfrac{\phi}{2}\left(\sin 2\tilde{\theta}\cos\tfrac{\phi}{2} + \cos 2\tilde{\theta}\sin\tfrac{\phi}{2}\sin\chi\right)^2}. \tag{16}$$

We can use this theoretical model for the DOP in (16) as well as the orientation of the output field in (6) to fit the experimental data and obtain the linear and circular birefringences.

B. Experimental sequences

The schematic time sequence for loading the HCPBGF with atoms is shown in Fig. 6(a).

The MOT is loaded for 990 ms with a Gaussian-shaped repumper beam in addition to a dark funnel repumper [33] to increase the number of atoms in the MOT. After the MOT loading phase the MOT repumper is switched off by a mechanical shutter and only the dark funnel repumper is left for increasing the density of atoms above the HCPBGF. Simultaneously, the current of the

Optics EXPRESS

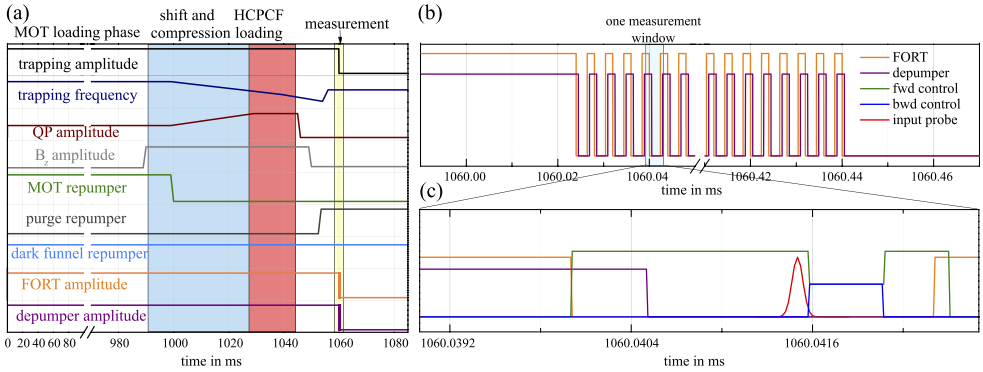

Fig. 6. (a) Time sequences of laser and magnetic fields for loading the HCPBGF with atoms. QP: quadrupole field of the MOT coils; B_z: magnetic offset field in the vertical direction that determines the zero point of the magnetic field and thereby shifts the atom cloud above the HCPBGF. (b) Sequence of the FORT and depumper for the SL/LSR/SLP experiments. (c) Sequence of the laser fields used for SL/LSR/SLP measurements.

quadrupole coils is doubled for compression of the cloud and the magnetic offset field in the $z-$direction (along the fiber axis) is changed to move the atoms towards the fiber tip. During the 40 ms long shift and compression and the 20 ms long HCPBGF loading phases, the trapping detuning is ramped from -2.5Γ to -5Γ for sub-Doppler cooling above the HCPBGF to increase the loading efficiency. During the HCPBGF loading phase the atoms are held above the HCPBGF where the FORT potential is strong enough to guide the atoms into the fiber. A depumper beam, tuned 133 MHz to the blue side of the transition $^2S_{1/2}$, $F = 2 \leftrightarrow {}^2P_{3/2}$, $F' = 2$, to account for the ac Stark shift by the FORT, is continuously on and serves to confine the atoms inside the dark funnel in $F = 1$ for enhancing the density near the fiber tip. Typically, 10^5 atoms are loaded into the HCPBGF.

After loading the HCPBGF is finished at 1050 ms and another 10 ms period for letting the quadrupole field decay, experimental runs of SL, LSR or SLPs start. The FORT (and the depumper) are rapidly switched on and off at a frequency of 250 kHz according to Fig. 6(b). This eliminates ac Stark shifts by the FORT during the measurement windows of 2.5 μs duration, but is still short enough to not lose a significant amount of atoms during this free expansion. Up to 50 measurements can be done with the same atoms loaded into the fiber, before losses became noticeable. In each time slot when the FORT is off, SL/LSR/SLP measurements [see Fig. 6(c)] are performed. The first 4 time slots are used to prepare the population in $F = 1$ by the control beam. We do not try to prepare the population in a single Zeeman level. Then, Gaussian probe pulses of $\tau_p = 150(2)$ ns $1/e$ full width are sent into the HCPBGF in the next 25 time slots. Afterwards, another 25 time slots are used to record the background signal without probe. Each HCPBGF loading cycle is followed by a reference measurement without atoms inside the HCPBGF, by keeping the MOT quadrupole field off. We therefore can detect the background due to the laser fields and due to scattered photons from the atoms inside the HCPBGF independently.

Funding

H2020 Marie Skłodowska-Curie Actions (765075).

Acknowledgments

The authors thank H.R. Hamedi, G. Birkl and M. Fleischhauer for helpful discussions, F. Blatt for assistance with measurements, and the group of T. Walther for providing us with a home-made ultra-low noise laser diode driver with high modulation bandwidth.

Optics EXPRESS

Disclosures

The authors declare no conflicts of interest.

References

1. M. A. Nielsen and I. L. Chuang, *Quantum computation and quantum information* (Cambridge University, 2001).
2. D. V. Strekalov and G. Leuchs, *Nonlinear Interactions and Non-classical Light* (Springer, Cham, 2019), pp. 51–101.
3. A. I. Lvovsky, B. C. Sanders, and W. Tittel, "Optical quantum memory," Nat. Photonics **3**(12), 706–714 (2009).
4. G. Brennen, E. Giacobino, and C. Simon, "Focus on Quantum Memory," New J. Phys. **17**(5), 050201 (2015).
5. D. E. Chang, V. Vuletić, and M. D. Lukin, "Quantum nonlinear optics - photon by photon," Nat. Photonics **8**(9), 685–694 (2014).
6. Y.-F. Hsiao, P.-J. Tsai, H.-S. Chen, S.-X. Lin, C.-C. Hung, C.-H. Lee, Y.-H. Chen, Y.-F. Chen, I. A. Yu, and Y.-C. Chen, "Highly efficient coherent optical memory based on electromagnetically induced transparency," Phys. Rev. Lett. **120**(18), 183602 (2018).
7. M. Fleischhauer, A. Imamoğlu, and J. P. Marangos, "Electromagnetically induced transparency: Optics in coherent media," Rev. Mod. Phys. **77**(2), 633–673 (2005).
8. J. L. Everett, D. B. Higginbottom, G. T. Campbell, P. K. Lam, and B. C. Buchler, "Stationary Light in Atomic Media," Adv. Quantum Technol. **2**(5-6), 1800100 (2019).
9. M. D. Lukin and A. Imamoğlu, "Controlling photons using electromagnetically induced transparency," Nature **413**(6853), 273–276 (2001).
10. M. D. Lukin and A. André, "Manipulating Light Pulses via Dynamically Controlled Photonic Band gap," Phys. Rev. Lett. **89**(14), 143602 (2002).
11. A. André, M. Bajcsy, M. D. Lukin, and A. S. Zibrov, "Nonlinear Optics with Stationary Pulses of Light," Phys. Rev. Lett. **94**(6), 063902 (2005).
12. D. E. Chang, V. Gritsev, G. Morigi, V. Vuletić, M. D. Lukin, and E. A. Demler, "Crystallization of strongly interacting photons in a nonlinear optical fibre," Nat. Phys. **4**(11), 884–889 (2008).
13. M. Hafezi, D. E. Chang, V. Gritsev, E. Demler, and M. D. Lukin, "Quantum transport of strongly interacting photons in a one-dimensional nonlinear waveguide," Phys. Rev. A **85**(1), 013822 (2012).
14. C. Noh and D. G. Angelakis, "Quantum simulations and many-body physics with light," Rep. Prog. Phys. **80**(1), 016401 (2017).
15. T. Chaneliére, D. N. Matsukevich, S. D. Jenkins, S.-Y. Lan, T. A. B. Kennedy, and A. Kuzmich, "Storage and retrieval of single photons transmitted between remote quantum memories," Nature **438**(7069), 833–836 (2005).
16. Y. Wang, J. Li, S. Zhang, K. Su, Y. Zhou, K. Liao, S. Du, H. Yan, and S.-L. Zhu, "Efficient quantum memory for single-photon polarization qubits," Nat. Photonics **13**(5), 346–351 (2019).
17. K.-K. Park, Y.-W. Cho, Y.-T. Chough, and Y.-H. Kim, "Experimental Demonstration of Quantum Stationary Light Pulses in an Atomic Ensemble," Phys. Rev. X **8**(2), 021016 (2018).
18. Y.-H. Chen, M.-J. Lee, W. Hung, Y.-C. Chen, Y.-F. Chen, and I. A. Yu, "Demonstration of the Interaction between Two Stopped Light Pulses," Phys. Rev. Lett. **108**(17), 173603 (2012).
19. A. V. Gorshkov, A. André, M. D. Lukin, and A. S. Sørensen, "Photon storage in Λ-type optically dense atomic media. II. Free-space model," Phys. Rev. A **76**(3), 033805 (2007).
20. S. Ghosh, A. R. Bhagwat, C. K. Renshaw, S. Goh, A. L. Gaeta, and B. J. Kirby, "Low-Light-Level Optical Interactions with Rubidium Vapor in a Photonic Band-Gap Fiber," Phys. Rev. Lett. **97**(2), 023603 (2006).
21. T. Takekoshi and R. J. Knize, "Optical Guiding of Atoms through a Hollow-Core Photonic Band-Gap Fiber," Phys. Rev. Lett. **98**(21), 210404 (2007).
22. M. Bajcsy, S. Hofferberth, V. Balić, T. Peyronel, M. Hafezi, A. S. Zibrov, V. Vuletić, and M. D. Lukin, "Efficient All-Optical Switching Using Slow Light within a Hollow Fiber," Phys. Rev. Lett. **102**(20), 203902 (2009).
23. B. Wu, J. F. Hulbert, E. J. Lunt, K. Hurd, A. R. Hawkins, and H. Schmidt, "Slow light on a chip via atomic quantum state control," Nat. Photonics **4**(11), 776–779 (2010).
24. S. Okaba, T. Takano, F. Benabid, T. Bradley, L. Vincetti, Z. Maizelis, V. Yampol'skii, F. Nori, and H. Katori, "Lamb-Dicke spectroscopy of atoms in a hollow-core photonic crystal fibre," Nat. Commun. **5**(1), 4096 (2014).
25. K. P. Nayak, M. Sadgrove, R. Yalla, F. L. Kien, and K. Hakuta, "Nanofiber quantum photonics," J. Opt. **20**(7), 073001 (2018).
26. A. Goban, C.-L. Hung, S.-P. Yu, J. Hood, J. Muniz, J. Lee, M. Martin, A. McClung, K. Choi, D. E. Chang, O. Painter, and H. J. Kimble, "Atom-light interactions in photonic crystals," Nat. Commun. **5**(1), 3808 (2014).
27. M. R. Sprague, P. S. Michelberger, T. F. M. Champion, D. G. England, J. Nunn, X.-M. Jin, W. S. Kolthammer, A. Abdolvand, P. S. J. Russell, and I. A. Walmsley, "Broadband single-photon-level memory in a hollow-core photonic crystal fibre," Nat. Photonics **8**(4), 287–291 (2014).
28. B. Gouraud, D. Maxein, A. Nicolas, O. Morin, and J. Laurat, "Demonstration of a Memory for Tightly Guided Light in an Optical Nanofiber," Phys. Rev. Lett. **114**(18), 180503 (2015).
29. C. Sayrin, C. Clausen, B. Albrecht, P. Schneeweiss, and A. Rauschenbeutel, "Storage of fiber-guided light in a nanofiber-trapped ensemble of cold atoms," Optica **2**(4), 353–356 (2015).

Optics EXPRESS

30. K. T. Kaczmarek, D. J. Saunders, M. R. Sprague, W. S. Kolthammer, A. Feizpour, P. M. Ledingham, B. Brecht, E. Poem, I. A. Walmsley, and J. Nunn, "Ultrahigh and persistent optical depths of cesium in Kagomé-type hollow-core photonic crystal fibers," Opt. Lett. **40**(23), 5582–5585 (2015).
31. A. P. Hilton, C. Perrella, F. Benabid, B. M. Sparkes, A. N. Luiten, and P. Light, "High-efficiency cold-atom transport into a waveguide trap," Phys. Rev. Appl. **10**(4), 044034 (2018).
32. R. F. Cregan, B. J. Mangan, J. C. Knight, T. A. Birks, P. S. J. Russell, P. J. Roberts, and D. C. Allan, "Single-Mode Photonic Band Gap Guidance of Light in Air," Science **285**(5433), 1537–1539 (1999).
33. F. Blatt, T. Halfmann, and T. Peters, "One-dimensional ultracold medium of extreme optical depth," Opt. Lett. **39**(3), 446–449 (2014).
34. E. Vetsch, S. T. Dawkins, R. Mitsch, D. Reitz, P. Schneeweiss, and A. Rauschenbeutel, "Nanofiber-based optical trapping of cold neutral atoms," IEEE J. Sel. Top. Quantum Electron. **18**(6), 1763–1770 (2012).
35. B. Debord, F. Amrani, L. Vincetti, F. Gérôme, and F. Benabid, "Hollow-Core Fiber Technology: The Rising of "Gas Photonics"," Fibers **7**(2), 16 (2019).
36. J. M. Fini, J. W. Nicholson, B. Mangan, L. Meng, R. S. Windeler, E. M. Monberg, A. DeSantolo, F. V. DiMarcello, and K. Mukasa, "Polarization maintaining single-mode low-loss hollow-core fibres," Nat. Commun. **5**(1), 5085 (2014).
37. P. J. Roberts, D. P. Williams, H. Sabert, B. J. Mangan, D. M. Bird, T. A. Birks, J. C. Knight, and P. S. J. Russell, "Design of low-loss and highly birefringent hollow-core photonic crystal fiber," Opt. Express **14**(16), 7329–7341 (2006).
38. G. Bouwmans, F. Luan, J. Knight, P. St. J. Russell, L. Farr, B. Mangan, and H. Sabert, "Properties of a hollow-core photonic bandgap fiber at 850 nm wavelength," Opt. Express **11**(14), 1613–1620 (2003).
39. F. Blatt, L. S. Simeonov, T. Halfmann, and T. Peters, "Stationary light pulses and narrowband light storage in a laser-cooled ensemble loaded into a hollow-core fiber," Phys. Rev. A **94**(4), 043833 (2016).
40. M. Wegmuller, M. Legré, N. Gisin, T. P. Hansen, C. Jakobsen, and J. Broeng, "Experimental investigation of the polarization properties of a hollow core photonic bandgap fiber for 1550 nm," Opt. Express **13**(5), 1457–1467 (2005).
41. F. Poletti, N. G. R. Broderick, D. J. Richardson, and T. M. Monro, "The effect of core asymmetries on the polarization properties of hollow core photonic bandgap fibers," Opt. Express **13**(22), 9115–9124 (2005).
42. K. Kikuchi and T. Okoshi, "Wavelength-sweeping technique for measuring the beat length of linearly birefringent optical fibers," Opt. Lett. **8**(2), 122–123 (1983).
43. G. Genov, T. E. Lellinger, T. Halfmann, and T. Peters, "Laser frequency stabilization by bichromatic saturation absorption spectroscopy," J. Opt. Soc. Am. B **34**(9), 2018–2030 (2017).
44. P. Palittapongarnpim, A. MacRae, and A. I. Lvovsky, "Note: a monolithic filter cavity for experiments in quantum optics," Rev. Sci. Instrum. **83**(6), 066101 (2012).
45. M. Fleischhauer and M. D. Lukin, "Dark-State Polaritons in Electromagnetically Induced Transparency," Phys. Rev. Lett. **84**(22), 5094–5097 (2000).
46. M. Fleischhauer and M. D. Lukin, "Quantum memory for photons: Dark-state polaritons," Phys. Rev. A **65**(2), 022314 (2002).
47. M. Bajcsy, A. S. Zibrov, and M. D. Lukin, "Stationary pulses of light in an atomic medium," Nature **426**(6967), 638–641 (2003).
48. F. E. Zimmer, A. André, M. D. Lukin, and M. Fleischhauer, "Coherent control of stationary light pulses," Opt. Commun. **264**(2), 441–453 (2006).
49. Y.-W. Lin, W.-T. Liao, T. Peters, H.-C. Chou, J.-S. Wang, H.-W. Cho, P.-C. Kuan, and I. A. Yu, "Stationary Light Pulses in Cold Atomic Media and without Bragg Gratings," Phys. Rev. Lett. **102**(21), 213601 (2009).
50. G. T. Campbell, Y.-W. Cho, J. Su, J. Everett, N. Robins, P. K. Lam, and B. C. Buchler, "Direct imaging of slow, stored and stationary EIT polaritons," Quantum Sci. Technol. **2**(3), 034010 (2017).
51. N. Lauk, C. O'Brien, and M. Fleischhauer, "Fidelity of photon propagation in electromagnetically induced transparency in the presence of four-wave mixing," Phys. Rev. A **88**(1), 013823 (2013).
52. A. Hilton, C. Perrella, A. Luiten, and P. Light, "Dual-Color Magic-Wavelength Trap for Suppression of Light Shifts in Atoms," Phys. Rev. Appl. **11**(2), 024065 (2019).
53. T. Yoon and M. Bajcsy, "Laser-cooled cesium atoms confined with a magic-wavelength dipole trap inside a hollow-core photonic-bandgap fiber," Phys. Rev. A **99**(2), 023415 (2019).
54. M. Xin, W. S. Leong, Z. Chen, and S.-Y. Lan, "Transporting Long-Lived Quantum Spin Coherence in a Photonic Crystal Fiber," Phys. Rev. Lett. **122**(16), 163901 (2019).
55. J. Flannery, R. Al Maruf, T. Yoon, and M. Bajcsy, "Fabry-Pérot Cavity Formed with Dielectric Metasurfaces in a Hollow-Core Fiber," ACS Photonics **5**(2), 337–341 (2018).
56. C.-L. Chen, *Foundations for Guided-Wave Optics* (John Wiley & Sons, Inc., Hoboken, NJ, USA, 2006).
57. W. J. Tabor and F. S. Chen, "Electromagnetic Propagation through Materials Possessing Both Faraday Rotation and Birefringence: Experiments with Ytterbium Orthoferrite," J. Appl. Phys. **40**(7), 2760–2765 (1969).